Accelerated heatwave trends from nonlinear land-atmosphere interactions in midlatitude humid regions

Text. S1. Comparison of the temperature decomposition based on XAI and surface energy perturbation

To attribute the temperature extremes to anomalies in the surface energy balance (Lee et al. 2017), we first write the energy balance as,

$$\boldsymbol{R_{ld} - R_{lu} + R_s - LE - SH = Q}, \qquad \text{Eq. S1}$$

where R_{ld} is the downward flux of longwave radiation, R_{lu} is the emitted upward flux of longwave radiation, R_s is the net absorption of solar radiation, LE is the latent heat flux, and H is the sensible heat flux, and Q is the ground heat flux. Note that the radiation terms are downward positive and turbulent heat fluxes are upward positive. By using $\sigma {T_s}^4$ for R_{lu} (with σ being the Stefan-Boltzmann constant and T_s the surface temperature), we can express ΔT_s as,

$$\boldsymbol{\Delta T_s = (\Delta R_{ld} + \Delta R_s - \Delta LE - \Delta H - \Delta Q)/4\sigma \overline{T_s}^3}. \qquad \text{Eq. S2}$$

In this surface energy balance framework, the effect of high pressure on temperature is majorly through an increase in solar radiation, which is represented by $C_{RS} = \frac{\Delta R_s}{4\sigma \overline{T_s}^3} / \boldsymbol{\Delta T_s}$. This can be interpreted as the marginal contribution of Z500 in the XAI framework, i.e., $C_{Z500} + \frac{C_{interact}}{2}$. Similarly, soil moisture primarily impacts temperature by decreasing latent heat flux, represented by $C_{LE} = \frac{-\Delta \mathrm{LE}}{4\sigma \overline{T_s}^3} / \boldsymbol{\Delta T_s}$,which can be interpreted as the marginal contribution of SM in the XAI framework, i.e., $C_{SM} + \frac{C_{interact}}{2}$. Note that the 'land-atmosphere' interaction, as assessed by quantifying the temperature difference with and without changes in soil moisture (Fischer et al., 2007), is conceptually similar to $C_{SM} + \frac{C_{interact}}{2}$.

Text. S2. Calculation of evaporative fraction and the evaporative-regime curve

Evaporative fraction (EF) and evaporative-regime are calculated following Fu et al. (2022). Evaporative fraction is the ratio of latent heat flux in the total turbulent flux, i.e.,

$$EF = \frac{LE}{LE+H}, \qquad \text{Eq. S2}$$

where LE and H are latent and sensible heat fluxes, respectively.

Following Fu et al. (2022), we calculate the evaporative-regime using summer EF and surface soil moisture (SM) by fitting the scattering of EF versus SM with a linear-plateau regression, i.e.,

$$EF = \begin{cases} k(SM - SM_0) + EF_0 & (SM < SM_0) \\ EF_0 & (SM \geq SM_0) \end{cases}, \qquad \text{Eq. S3}$$

Table. S1. Model evaluation in Central Europe

	R2-score	**90th error (K)**	**MAE (K)**	**MSE (K^2)**
Main setting	0.78	-0.73	1.03	1.67
with XGBoost	0.77	-0.73	1.03	1.67
with Eobs	0.80	-0.67	1.08	1.81

Table. S2. CMIP6 climate model information

model	**Variant label**	**experiment**	**period**
Ec-Earth3	r1i1p1f1	Historical + ssp370	1979-2023
NorESM2-MM	r1i1p1f1	Historical + ssp370	1979-2023
NorESM2-LM	r1i1p1f1	Historical + ssp370	1979-2023
ACCESS-CM2	r1i1p1f1	Historical + ssp370	1979-2023
CanESM5	r1i1p1f1	Historical + ssp370	1979-2023
IPSL-CM6A-LR	r1i1p1f1	Historical + ssp370	1979-2023
MPI-ESM1-2-HR	r1i1p1f1	Historical + ssp370	1979-2023
MPI-ESM1-2-LR	r1i1p1f1	Historical + ssp370	1979-2023
UKESM1-0-LL	r1i1p1f1	Historical + ssp370	1979-2023
INM-CM4-8	r1i1p1f1	Historical + ssp370	1979-2023
INM-CM5-0	r1i1p1f1	Historical + ssp370	1979-2023
MIROC6	r1i1p1f1	Historical + ssp370	1979-2023

Table. S3. CESM2-LE2 40 members information

Variant label	**experiment**	**period**	**Forcing**
1231.01	Historical + ssp370	1979-2023	CMIP6 BMB forcing
1231.02	Historical + ssp370	1979-2023	CMIP6 BMB forcing
1231.03	Historical + ssp370	1979-2023	CMIP6 BMB forcing
1231.04	Historical + ssp370	1979-2023	CMIP6 BMB forcing
1231.05	Historical + ssp370	1979-2023	CMIP6 BMB forcing
1231.06	Historical + ssp370	1979-2023	CMIP6 BMB forcing
1231.07	Historical + ssp370	1979-2023	CMIP6 BMB forcing
1231.08	Historical + ssp370	1979-2023	CMIP6 BMB forcing
1231.09	Historical + ssp370	1979-2023	CMIP6 BMB forcing
1231.10	Historical + ssp370	1979-2023	CMIP6 BMB forcing
1251.01	Historical + ssp370	1979-2023	CMIP6 BMB forcing
1251.02	Historical + ssp370	1979-2023	CMIP6 BMB forcing

1251.03	Historical + ssp370	1979-2023	CMIP6 BMB forcing
1251.04	Historical + ssp370	1979-2023	CMIP6 BMB forcing
1251.05	Historical + ssp370	1979-2023	CMIP6 BMB forcing
1251.06	Historical + ssp370	1979-2023	CMIP6 BMB forcing
1251.07	Historical + ssp370	1979-2023	CMIP6 BMB forcing
1251.08	Historical + ssp370	1979-2023	CMIP6 BMB forcing
1251.09	Historical + ssp370	1979-2023	CMIP6 BMB forcing
1251.10	Historical + ssp370	1979-2023	CMIP6 BMB forcing
1281.01	Historical + ssp370	1979-2023	CMIP6 BMB forcing
1281.02	Historical + ssp370	1979-2023	CMIP6 BMB forcing
1281.03	Historical + ssp370	1979-2023	CMIP6 BMB forcing
1281.04	Historical + ssp370	1979-2023	CMIP6 BMB forcing
1281.05	Historical + ssp370	1979-2023	CMIP6 BMB forcing
1281.06	Historical + ssp370	1979-2023	CMIP6 BMB forcing
1281.07	Historical + ssp370	1979-2023	CMIP6 BMB forcing
1281.08	Historical + ssp370	1979-2023	CMIP6 BMB forcing
1281.09	Historical + ssp370	1979-2023	CMIP6 BMB forcing
1281.10	Historical + ssp370	1979-2023	CMIP6 BMB forcing
1301.01	Historical + ssp370	1979-2023	CMIP6 BMB forcing
1301.02	Historical + ssp370	1979-2023	CMIP6 BMB forcing
1301.03	Historical + ssp370	1979-2023	CMIP6 BMB forcing
1301.04	Historical + ssp370	1979-2023	CMIP6 BMB forcing
1301.05	Historical + ssp370	1979-2023	CMIP6 BMB forcing
1301.06	Historical + ssp370	1979-2023	CMIP6 BMB forcing
1301.07	Historical + ssp370	1979-2023	CMIP6 BMB forcing
1301.08	Historical + ssp370	1979-2023	CMIP6 BMB forcing
1301.09	Historical + ssp370	1979-2023	CMIP6 BMB forcing
1301.10	Historical + ssp370	1979-2023	CMIP6 BMB forcing

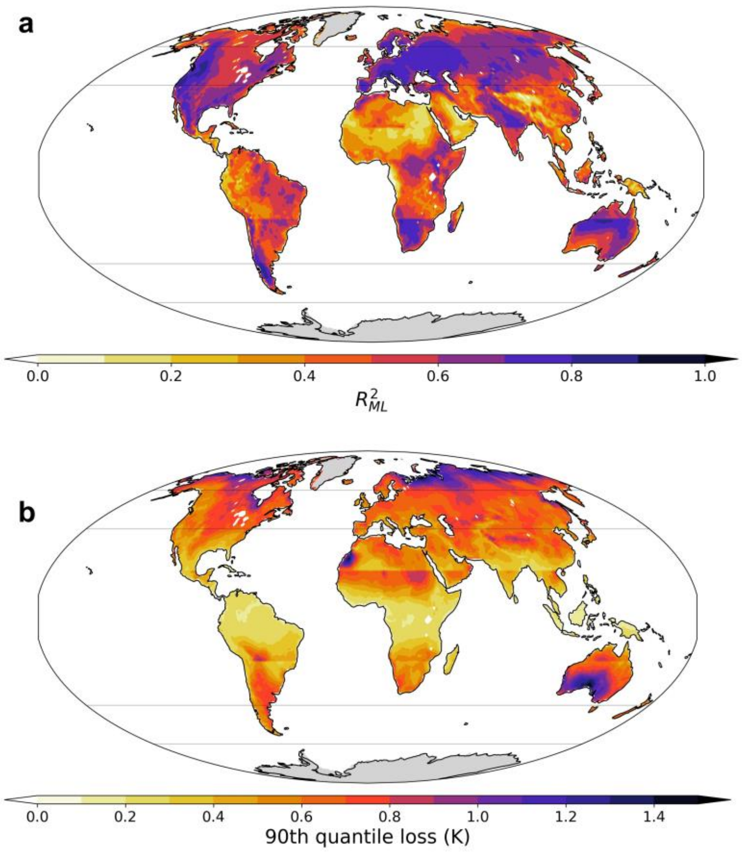

Figure S1. GradiantBoostingRegressor ML Model evaluation in global scale. (a) $\mathrm{R}^2-\mathrm{score}$ of the GradiantBoostingRegressor ML Model predicted T_x and the ERA5-land T_x during summer 1979−2023. **(b)** The 90th quantile loss of the GradiantBoostingRegressor ML Model predicted Tx during summer 1979−2023. The horizontal grey lines represent midlatitude (40° −60°).

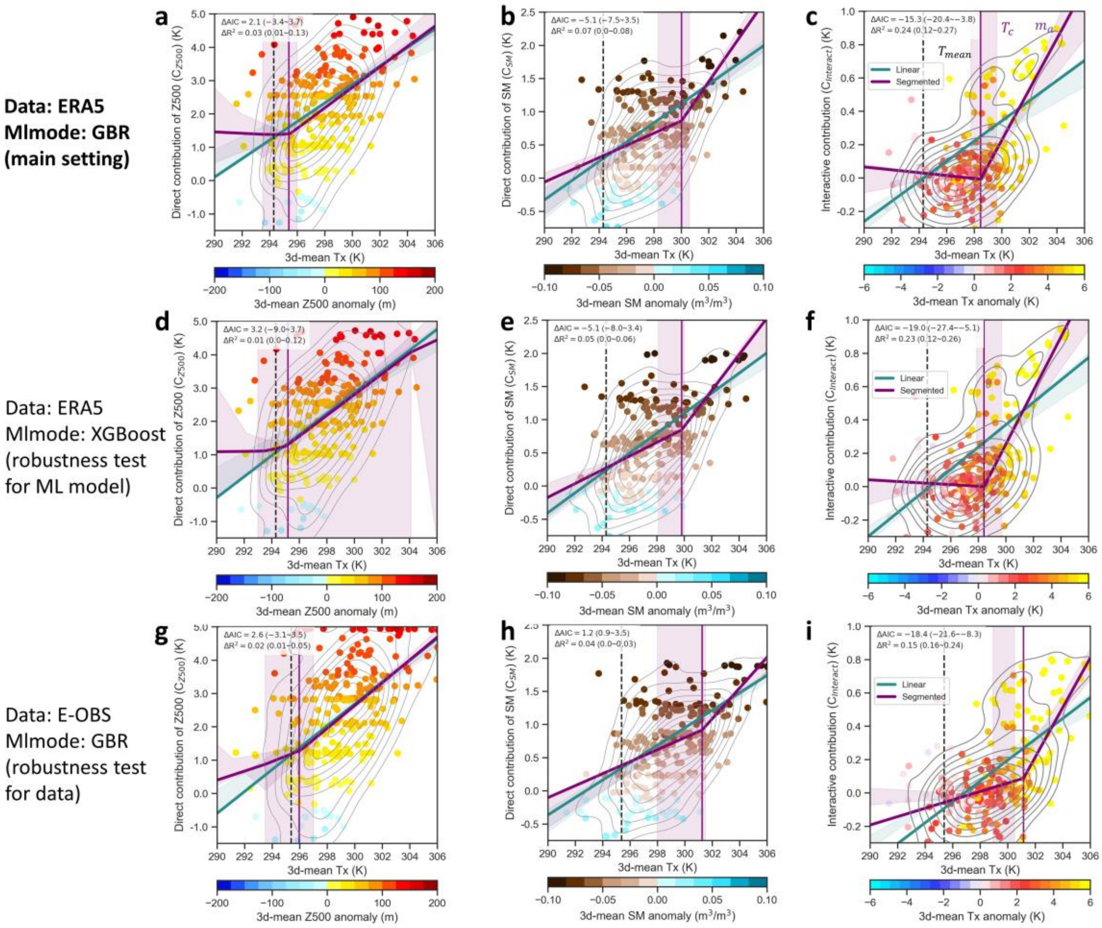

Figure. S2. Regression of the Central-Europe-mean T_x and the corresponding decompositions, namely, **(a,d,g)** C_{Z500}, **(b,e,h)** C_{SM}, and **(c,f,i)** $C_{Interact}$ for all summer heatwave periods in Central Europe from 1979 to 2023, using (**a,b,c**) ERA5 data+GBR ML model, (**d,e,f**) ERA5 data+XGBoost ML model, (**g,h,i**) E-obs data+GBR ML model**.** Contours represent the kernel density estimation, with levels ranging from 0.1 to 0.9; the envelope indicate the 99% confidence interval; ΔAIC and ΔR^2 are the performance difference between the segmented and linear regression, with the 99% confidence interval (LCI–UCI) provided; T_{mean} is the multiyear-mean summer T_x; T_c is the critical temperature; m_a is the slope of dependence between contributor and temperature in critical regime.

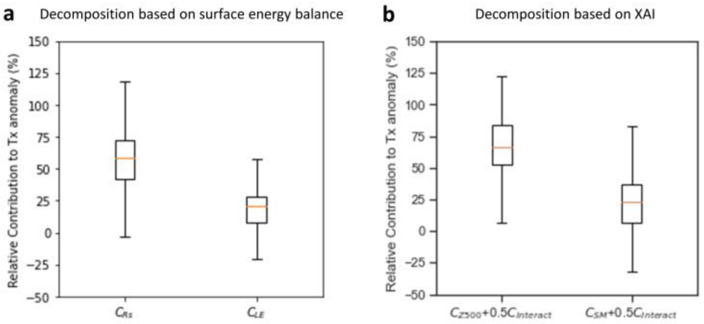

$$C_{RS} = \frac{\Delta R_S}{4\sigma \bar{T_S}^3} / \Delta T_S \qquad C_{LE} = \frac{-\Delta LE}{4\sigma \bar{T_S}^3} / \Delta T_S$$

$$\Delta T_S = \underbrace{\frac{\Delta R_S}{4\sigma \bar{T_S}^3}}_{\text{Shortwave radiation}} + \underbrace{\frac{\Delta R_{ld}}{4\sigma \bar{T_S}^3}}_{\text{longwave down}} + \underbrace{\frac{-\Delta LE}{4\sigma \bar{T_S}^3}}_{\text{latent}} + \underbrace{\frac{-\Delta H}{4\sigma \bar{T_S}^3}}_{\text{sensible}} + \underbrace{\frac{\Delta Q}{4\sigma \bar{T_S}^3}}_{\text{ground heat}}$$

Figure S3. **Contribution of atmospheric and surface drivers to summer heatwaves in Central Europe:** Insights from **(a)** Surface Energy Balance Perturbation and **(b)** Explainable AI (XAI).

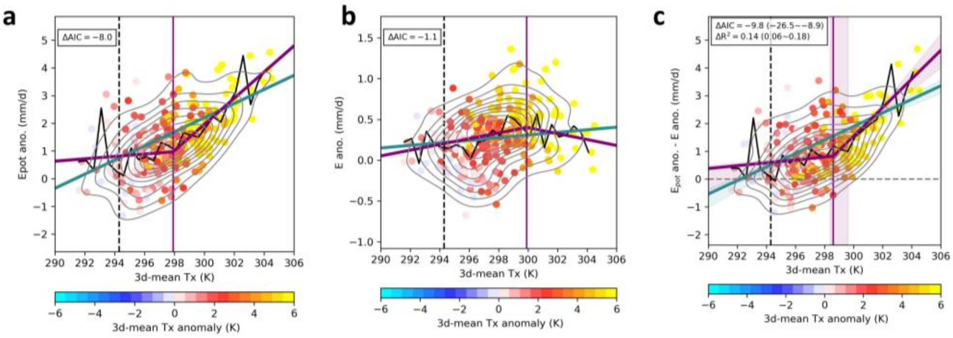

Figure. S4. Interpretation of the nonlinearity of the interaction in Central Europe based on potential evaporation anomaly and evaporation anomaly. Regression of the Central-Europe-mean T_x and **(a)** potential evaporation anomaly (E_{pot} ano.); **(b)** evaporation anomaly (E ano.); **(c)** difference between potential evaporation anomaly (E_{pot} ano.) and evaporation anomaly (E ano.) for all summer heatwave periods in Central Europe from 1979 to 2023.

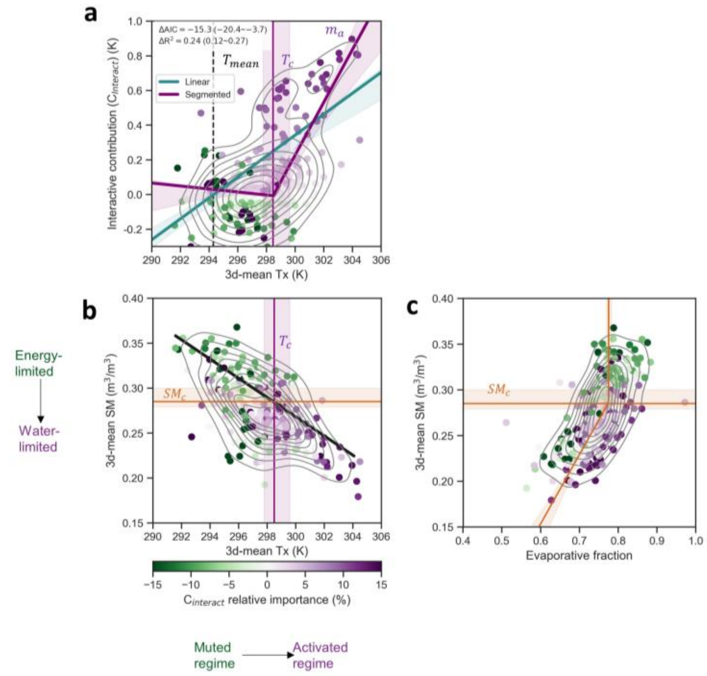

Figure. S5. Regression analyses over 1979–2023 summers during heatwave period in central Europe: **(a)** segmented regression between $C_{Interact}$ and T_x; **(b)** linear regression between T_x and SM; **(d)** segmented regression between SM vs. EF. Contours represent the kernel density estimation, with levels ranging from 0.1 to 0.9; shaded envelope indicates the 99% confidence interval of the segmented and linear fitting; ΔAIC and ΔR^2 are the performance difference between the segmented and linear regression, with the 99% confidence interval (LCI–UCI) provided; T_{mean} is the multiyear-mean summer T_x; T_c is the critical temperature marking shift of land-atmosphere interaction from muted to activate regime; m_a is the slope of dependence between T_x and $C_{Interact}$ in activated regime; SM_c is the critical soil moisture marking transition between energy- to water- limited evaporation.

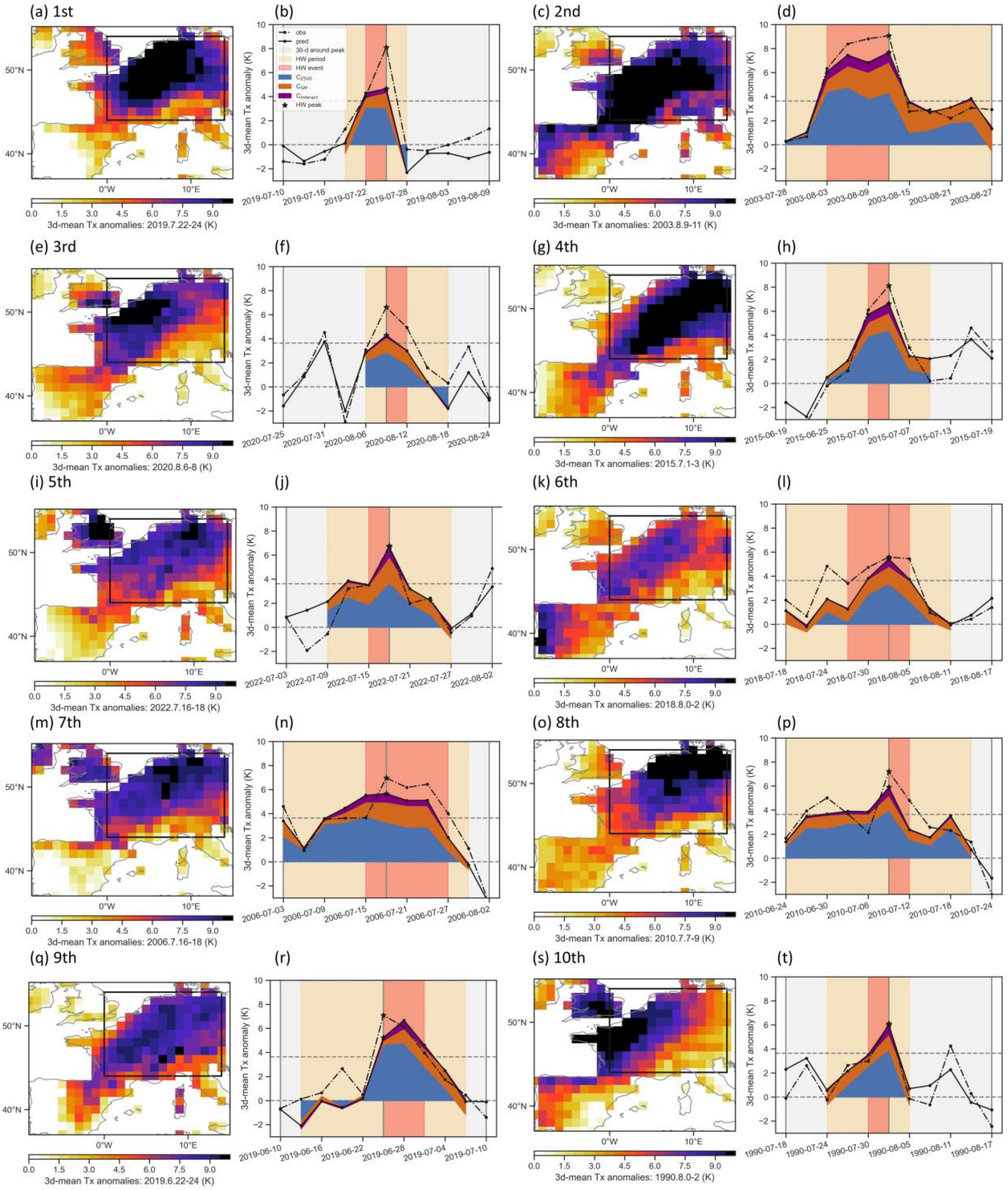

Figure. S6. Top 10 heatwave event in Central Europe. Similar to Fig. 1a-b but for top 10 heatwaves in Central Europe during 1979~2023 summer.

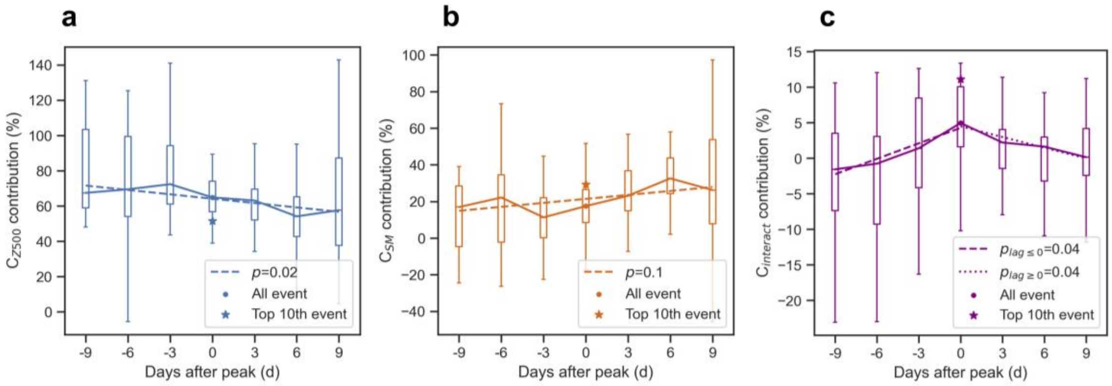

Figure. S7. Evolution of heatwave events. The three components before and after heatwave peak in Central Europe during summer, composited of all summer heatwaves during 1979~2023.

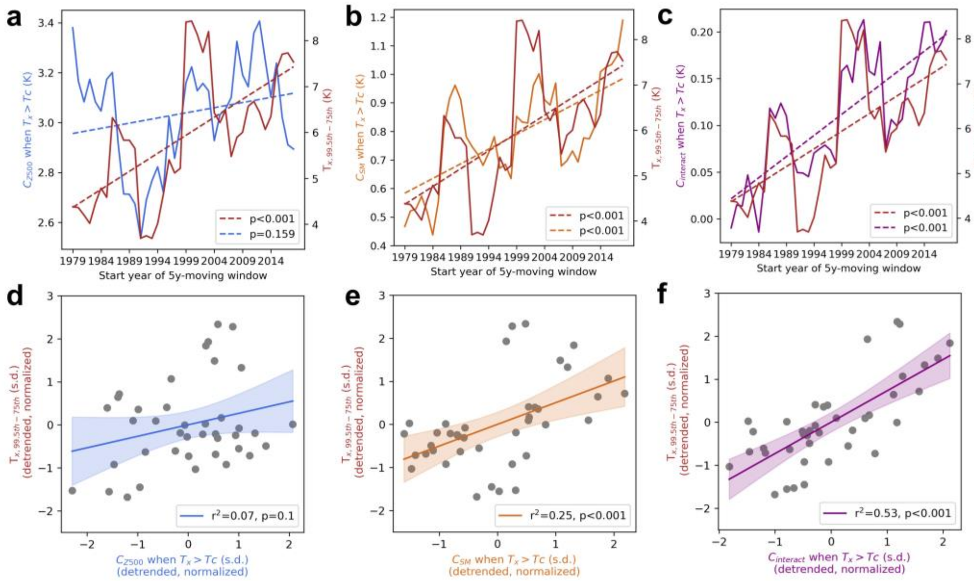

Figure. S8. Relationship changes in T_x tail width ($T_{x,99.5th} - T_{x,75th}$) and three components in Central Europe during summer heatwave period in 1979~2023. (a-c) The 5y-moving window T_x tail width ($T_{x,99.5th} - T_{x,75th}$) in Central Europe during summer heatwave period in 1979~2023 and the 5y-moving window average **(a)** C_{Z500}, **(b)** C_{SM}, and **(c)** $C_{interact}$. **(d-f)** The regression between the 5y-moving window T_x tail width ($T_{x,99.5th} - T_{x,75th}$) in Central Europe during summer heatwave period in 1979~2023 and the 5y-moving window average **(d)** C_{Z500}, **(e)** C_{SM}, and **(f)** $C_{interact}$, with all time series detrended.

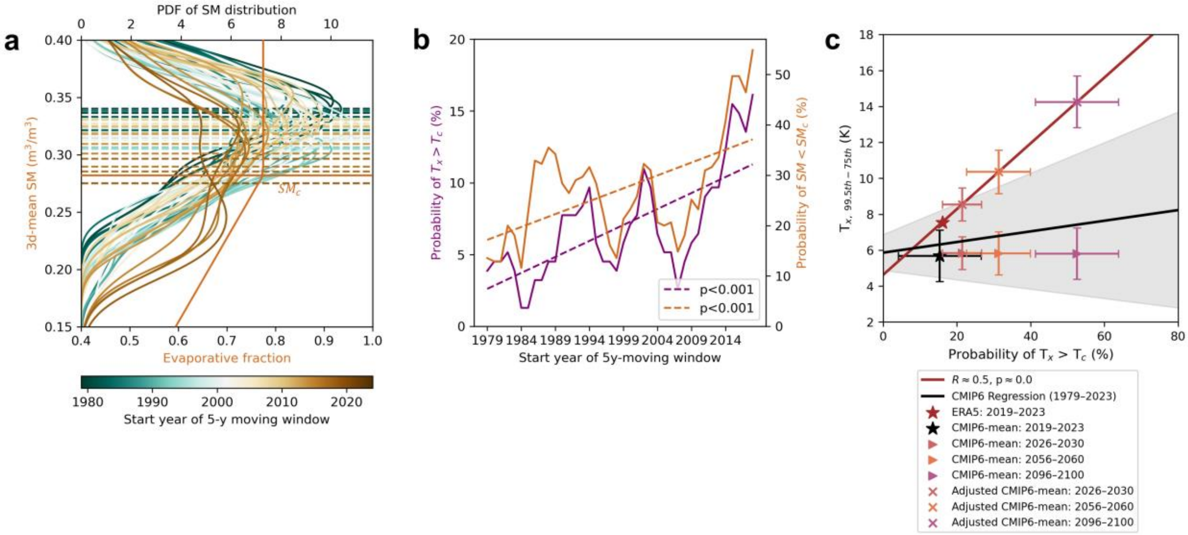

Figure. S9. An increasing probability of exceeding the critical temperature enhances land-atmosphere interactions, thereby widening the upper tail of the temperature distribution in Central Europe. (a) The changes in 5year-moving window SM distribution, **(b)** The changes in 5year-moving window probability of $T_x > T_{c,interact}$ during summer in Central Europe. **(c)** Linear regression between 5year-moving window upper tail width of temperature ($T_{x,99.5th} - T_{x,75th}$) and critical threshold exceedance frequency (probability of $T_x > T_{c,interact}$) in ERA5 and climate models.

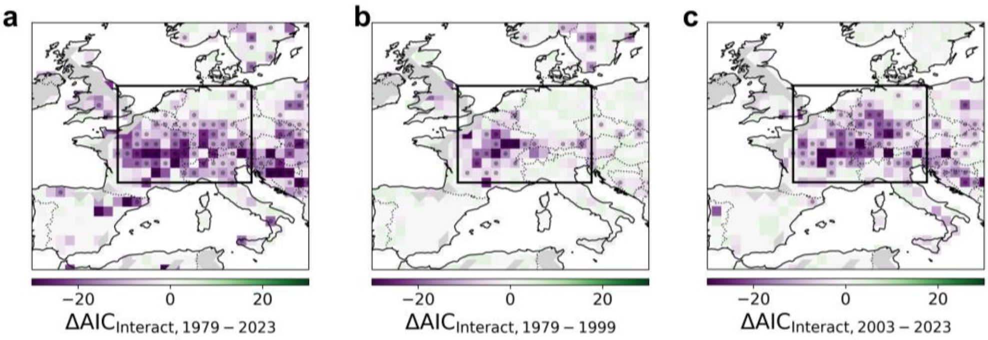

Figure. S10. Expansion of the affected region of nonlinear interaction in western Europe. The nonlinearity of interactive contribution during summer heatwaves in 1979~2023, **(b)** 1979~1999, and **(c)** 2003~2023.

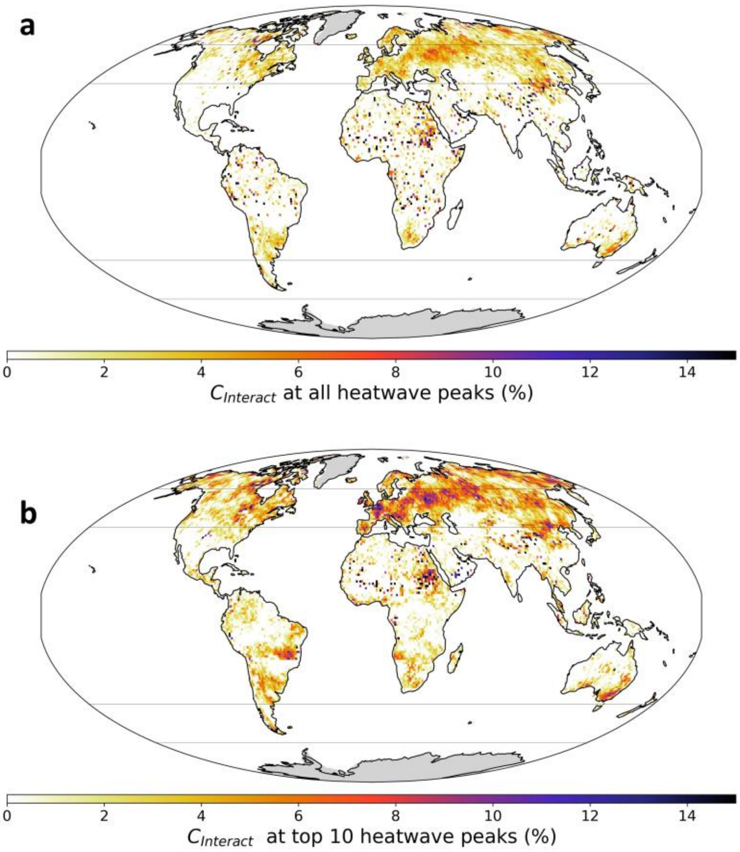

Figure S11. Contribution of interactive contribution to (a) all summer heatwave peaks from 1979~2023 and to **(b)** the top 10 summer heatwave peaks.

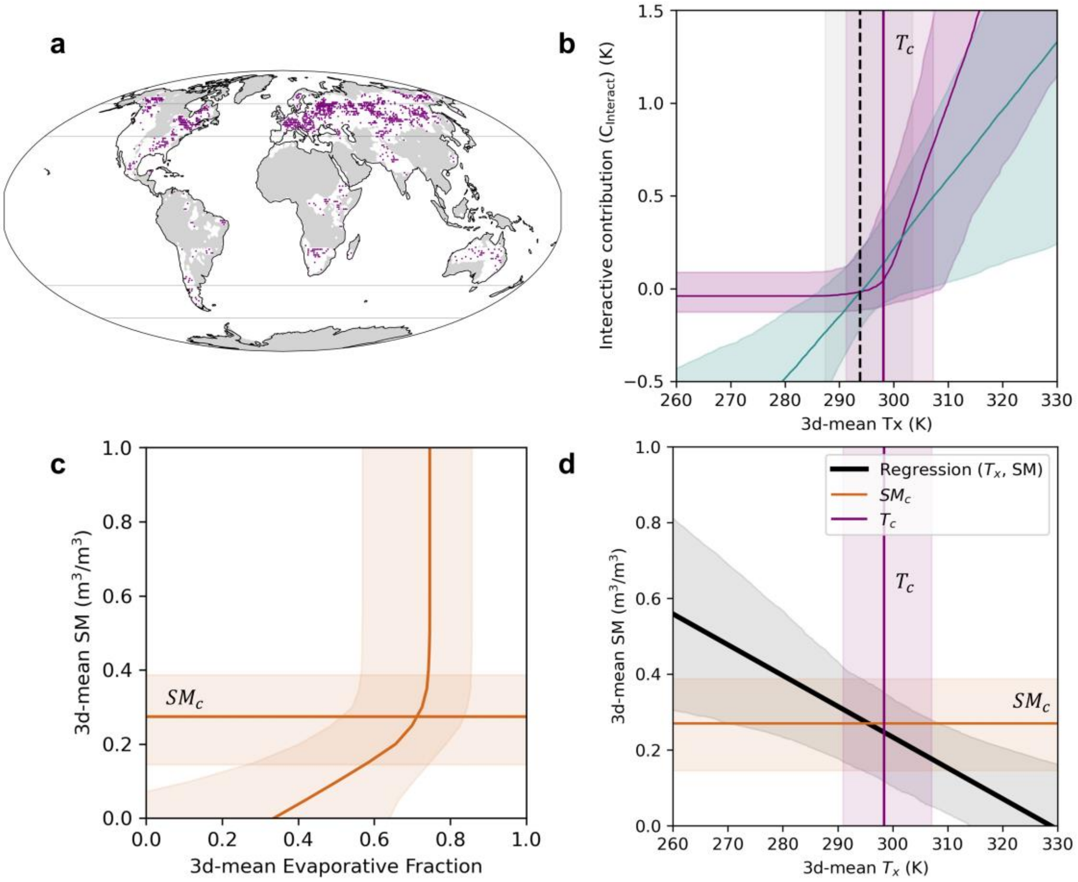

Figure S12. (a) Locations with significant nonlinear land-atmosphere interaction. **(b-d)** Spatially-composited regression analyses over 1979–2023 summers during heatwave period in midlatitude humid region: **(b)** segmented regression between $C_{Interact}$ and T_x ; **(c)** segmented regression between SM and EF; **(d)** linear regression between T_x and soil moisture.

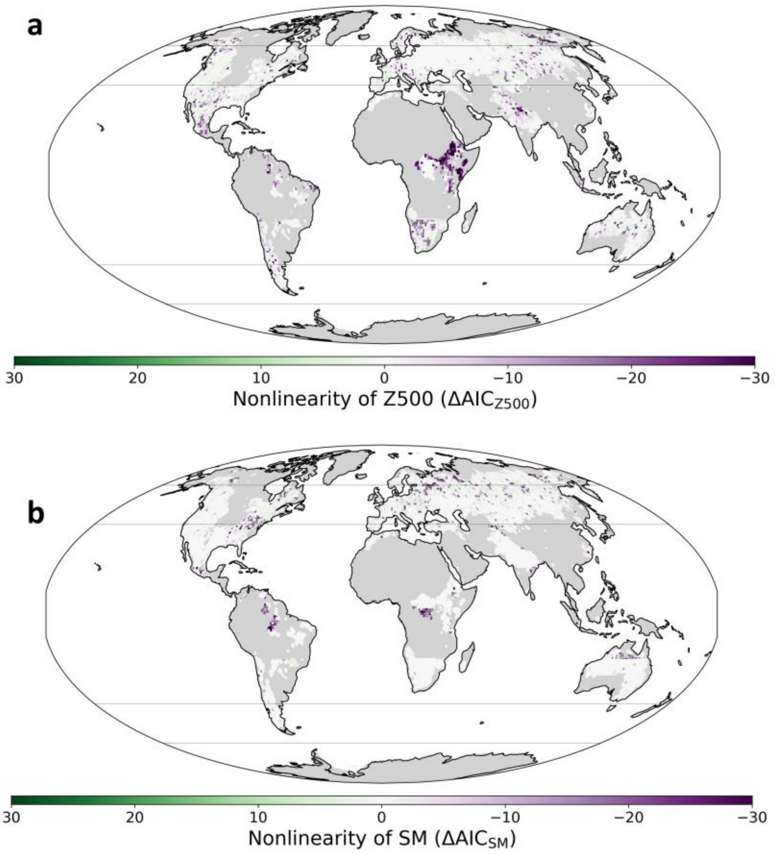

Figure S13. Nonlinearity magnitude of (a) direct contribution of *Z500* and (b) direct contribution of *SM* during summer HW period 1979-2023, with black dot presenting significantly nonlinear interaction**.** The grey area indicates $R_{ML}^2 < 0.6$.

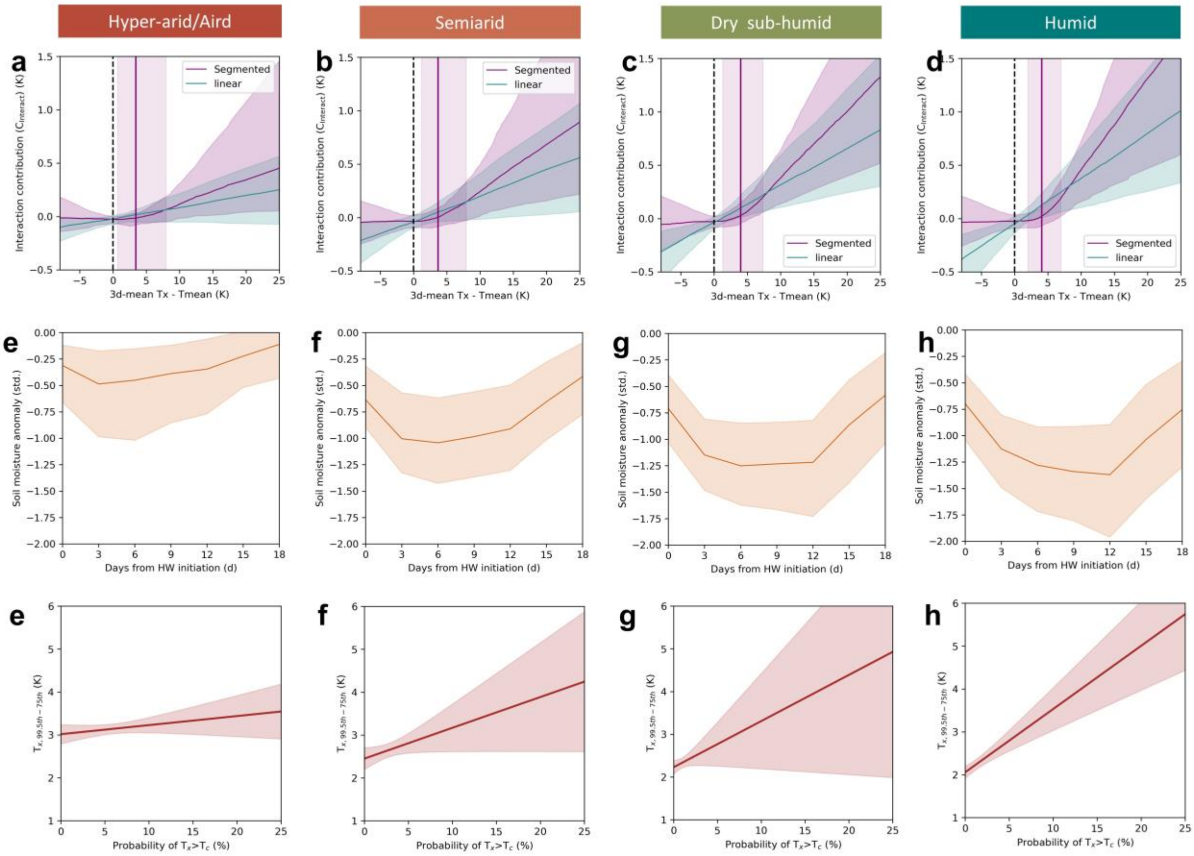

Figure S14. The composite of the nonlinear relationship between $C_{Interact}$ and T_x during summer HW period 1979-2023 classified by aridity index (the first row). The standardized soil moisture anomaly during summer HW period 1979-2023 classified by aridity index (the second row). The linear regression between 5year-moving window upper tail width of temperature ($T_{x,99.5th} - T_{x,75th}$) and critical threshold exceedance frequency (probability of $T_x > T_{c,interact}$). (The third row). The envelope indicates the 5th to 95th percentile of the variation among the grids.

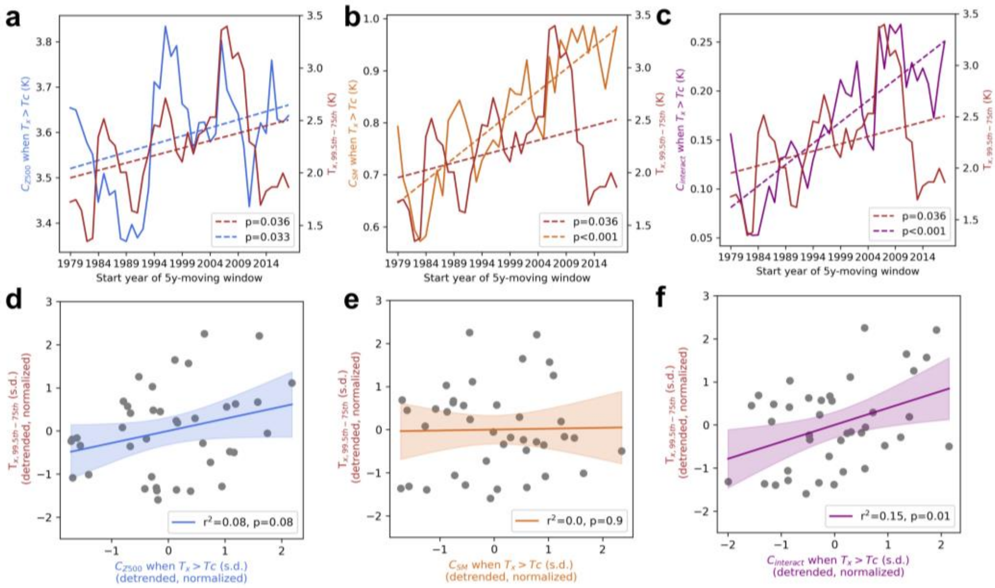

Figure S15. The same as Figure. S8 but for midlatitude humid zones.

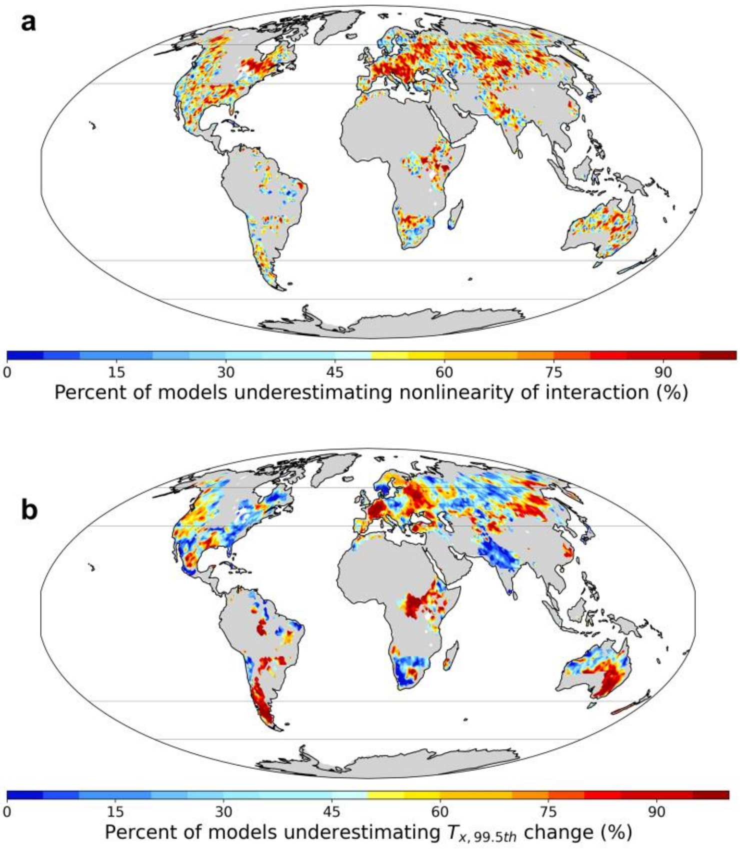

Figure S16. Percent of CMIP6 models underestimating (a) the nonlinearity magnitude of interactive contribution ($\Delta AIC_{interact,ERA5} < \Delta AIC_{interact,CMIP6}$) during 1979-2023 summer HW period and **(b)** change of $T_{x,99.5th}$ in summer (2004~2023 compared with 1979~1998). The grey area indicates $R^2_{ML} < 0.6$, and the grey lines indicate midlatitude (40°~60°).

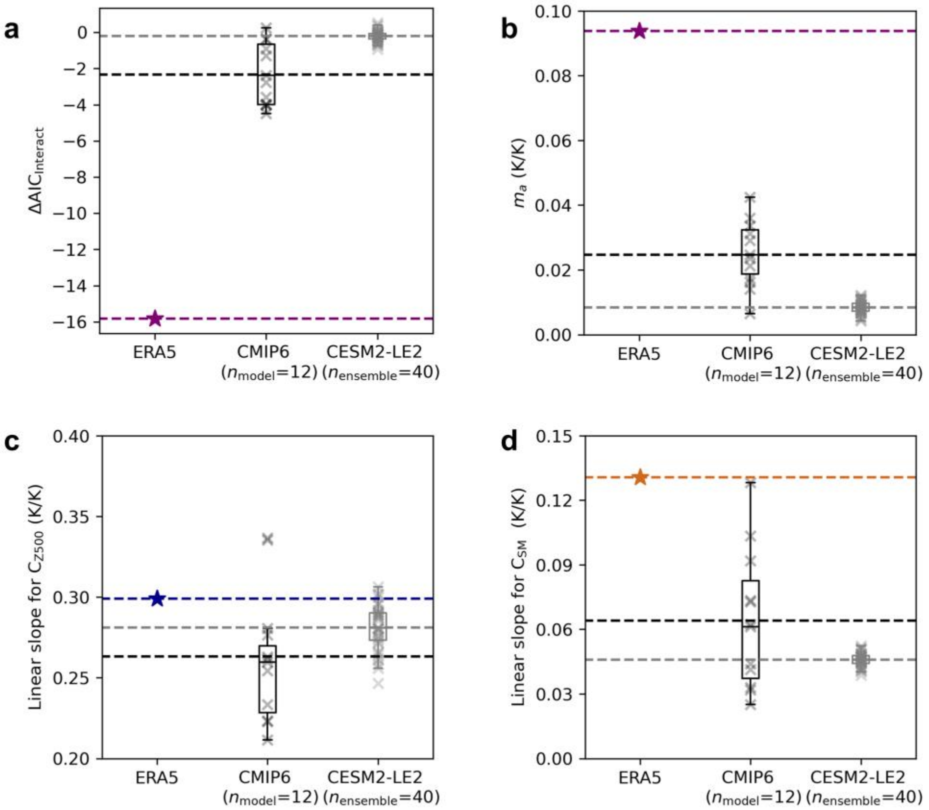

Figure S17. **CMIP6 model bias in nonlinear interaction during heatwaves**. Difference between ERA5, CMIP6 models, and CESM2-LE2 ensembles at locations with observed significant nonlinear interaction in **(a)** nonlinearity magnitude of $C_{Interact}$ ($\Delta AIC_{interact}$), **(b)** slope of dependence between $C_{Interact}$ and T_x (m_a), **(c)** linear slope between C_{Z500} and T_x, and **(d)** linear slope between C_{SM} and T_x during 1979-2023 summer HW period. The metrics are initially calculated for each grid, and the median value among the grids is subsequently presented for each model/ensemble. Boxes display 25th and 75th percentile while the median is shown as a horizontal black line. The whiskers denote the 5th and 95th percentile.

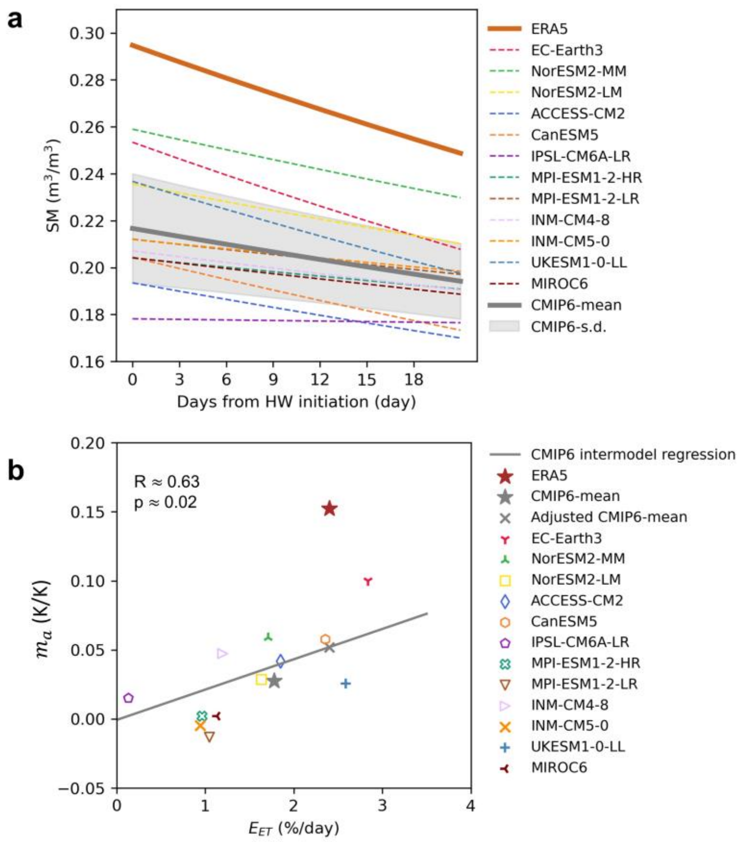

Figure S18. Soil moisture response at the initial stage of heatwaves in central Europe in (a) observation and CMIP6 models. (b) Regression between the soil moisture decline rate during heatwaves (E_{ET}) and (m_a) across climate models.

Reference

Fischer, E. M., S. I. Seneviratne, D. Lüthi, and C. Schär (2007), Contribution of land-atmosphere coupling to recent European summer heat waves, Geophys. Res. Lett., 34, L06707, doi:10.1029/2006GL029068.

Fu et al. Critical soil moisture thresholds of plant water stress in terrestrial ecosystems.Sci. Adv.8,eabq7827(2022). DOI:10.1126/sciadv.abq7827

Lee, S., et al., Revisiting the Cause of the 1989–2009 Arctic Surface Warming Using the Surface Energy Budget: Downward Infrared Radiation Dominates the Surface Fluxes. Geophysical Research Letters, 2017. 44(20): p. 10,654-10,661.